


Seven-Component Decomposition Using Refined Volume Scattering Models and New Configurations of Mixed Dipoles

Yu Wang , *Student Member, IEEE*, Weidong Yu, *Member, IEEE*, Xiuqing Liu, and Chunle Wang

Abstract—In this article, an extended seven-component decomposition method using refined volume scattering models and new configurations of mixed dipoles (M7SD) is proposed to interpret the scattering mechanisms of various terrain types. In the M7SD, refined volume scattering models are proposed to reasonably characterize the scattering mechanisms of various land covers with different orientation angles, and the redefined configurations of the mixed dipoles, which have better explanations for the scattering mechanisms, are introduced. Although the diameter of the dipole used in the experiment is very small, the superposition of two dipoles in the same plane will cause one of the dipoles to have a distance from the plane. According to the experimental results, since the distance between one of the dipoles and plane cannot be ignored, it will cause an error between the scattering matrix obtained by the experiment and the scattering matrix obtained under ideal conditions. In this case, in the M7SD, two dipoles are placed in two planes, respectively, with a distance of half wavelength. The performance of the proposed method is demonstrated and evaluated with the spaceborne C-band GaoFen-3, Radarsat-2, and airborne L-band ESAR fully polarimetric data over different study sites. The experimental results demonstrate that the use of the M7SD can reasonably interpret the scattering mechanisms of various terrain types (especially the building areas with large orientation angles), overcome the overestimation of the volume scattering and reduce the percentage of negative scattering power pixels.

Index Terms—Model-based decomposition, new configurations of compound scattering matrices, polarimetric synthetic aperture radar (PolSAR), refined volume scattering models.

I. INTRODUCTION

WITH the development of the synthetic aperture radar (SAR), polarimetric SAR (PolSAR) has been applied in

Manuscript received March 12, 2020; revised June 17, 2020 and July 11, 2020; accepted July 20, 2020. Date of publication July 24, 2020; date of current version August 14, 2020. This work was supported in part by the National Key Research and Development Program of China under Grant 2017YFB0502700, in part the Natural Science Foundation of Beijing Municipality under Grant 4192065, and in part by the Civil Aerospace Pre-research Project under Grant D040114. (*Corresponding author: Yu Wang.*)

Yu Wang and Weidong Yu are with the Department of Space Microwave remote Sensing System, Aerospace Information Research Institute, Chinese Academy of Sciences, Beijing 100190, China, and also with the University of Chinese Academy of Sciences, Beijing 100039, China (e-mail: wangyu370705@163.com; ywd@mail.ie.ac.cn).

Xiuqing Liu and Chunle Wang are with the Department of Space Microwave remote Sensing System, Aerospace Information Research Institute, Chinese Academy of Sciences, Beijing 100190, China (e-mail: lucia@mail.ie.ac.cn; clwang@mail.ie.ac.cn).

Digital Object Identifier 10.1109/JSTARS.2020.3011735

many fields [1]–[12]. Among them, polarimetric target decomposition plays an important role in interpreting the scattering mechanisms of various land covers. The existing incoherent target decomposition methods can be classified into three categories, namely, model-based decomposition, eigenvalue-based decomposition, and the hybrid decomposition categories. These decomposition algorithms are summarized in [13]. With the ensemble average employed, the eigenvalue-based decomposition method decomposes the coherency matrix into three orthogonal components. The foundation method was proposed by Cloude and Pottier [14] and has been employed by many researchers [15], [16]. However, among the existing methods, because of the simplicity and generality, the model-based methods are used universally.

The first model-based decomposition method was proposed by Freeman and Durden (FDD) [17], which divides the image into three scattering mechanisms including surface scattering based on a small perturbation model, double-bounce scattering derived from a dihedral corner reflector, and volume scattering modeled by a cloud of randomly oriented dipoles. The method decomposes the image using the polarimetric backscatter from naturally occurring scatterers. However, this approach overestimates the volume scattering power (OVS). With the development of the model-based decomposition, extended scattering mechanisms, such as helix [18], [19], wire [20], cross [21], compound dipole scattering [22], etc., have been proposed to overcome the OVS.

In the last decades, several decomposition methods have been widely used. The method with and without orientation angle compensation (OAC) proposed by Yamaguchi *et al.* [18], [19] takes helix scattering component into consideration. In this case, the scattering mechanism of urban area can be characterized. The phase angle compensation proposed by Singh *et al.* (G4U) [23] was also added to the decomposition method to overcome the OVS. Accordingly, helix angle compensation (HAC) was introduced by Quan *et al.* [24]. With this compensation, the contribution of volume scattering can be further reduced. All the previously described four-component decomposition methods are proposed under the assumption of reflection symmetry, which is the major drawback of model-based decomposition. Since the cross- and copolarization is considered to be irrelative, the T_{13} and T_{23} terms are forced to zero. However, PolSAR data cannot always satisfy this assumption and the polarimetric information cannot be fully utilized. In addition to the vegetation

areas, the oriented buildings also contribute to the cross-pol HV scattering, thereby, leading to substantial volume scattering. Li *et al.* demonstrate that the helix component can mitigate some of the impacts of the reflection symmetry while generating some negative power problems [25]. To further overcome the OVS, a six-component decomposition method (6SD) was proposed by Singh *et al.* that also considers oriented dipoles and compound scattering component [22]. The decomposition results obtained via this method are consistent with the terrain types, including ocean, forests, and buildings orthogonal to the radar line of sight (orthogonal buildings). The volume scattering component of the oriented buildings can also be effectively reduced.

When the rotation angle between the vertical wall of the oriented building and the flight direction is small, the OAC can effectively reduce the cross-pol power by minimizing the term T_{33} in the coherency matrix. However, when this rotation angle exceeds a specified range, the OAC is no longer effective, and the oriented building induces a strong cross-pol power contribution [26], [27].

The preferential calculation of the volume scattering and other scattering components (i.e., helix scattering, wire scattering, and compound scattering, etc.) leads to the occurrence of the negative power pixels. In the model-based decomposition methods, the surface/double-bounce scattering is assumed to be 0 when the power value is less than 0, resulting in the misinterpretation of the surface/double-bounce scattering. Although the OAC can be used to reduce the number of negative pixels by reducing the value of T_{33} element to less than that of T_{22} , the T_{33} value of pixels with large T_{33} values in the forests will be mistakenly reduced [25], [28]. Therefore, the OAC is effective only within a certain range of rotation angle. In this case, a seven-component decomposition method was proposed by Singh *et al.* (7SD), where the OAC is not introduced [29]. In this method, all elements of the coherency matrix can be considered. The rotation of the coherency matrix is not required by the 7SD and the original data matrix can be preserved. The performance of this method has been demonstrated and the decomposition results can be used to characterize the scattering mechanisms of various land covers. Although the models can illustrate the real and imaginary parts of T_{13} and T_{23} mathematically, the physical meanings corresponding to these models are not clear. Since the T_{13} and T_{23} are the Pauli-based coupling terms, two coupling scattering components are proposed in this article to characterize the physical meanings of these coupling terms. If the cross- and copolarization are irrelevant, these coupling terms are forced to zero; otherwise, these coupling models can be used to reflect the coupling information.

In this article, according to the 7SD, an extended seven-component decomposition method with refined volume scattering models and new configurations of mixed dipoles (M7SD) is proposed. Compared with the 7SD, the contributions of this method are as follows

1) The refined volume scattering models considering orientation angles of various terrain types are proposed. These refined models can be used to effectively characterize the volume scattering component of various land covers, especially the building areas with large orientation angles.

2) The configurations of mixed dipoles are redefined. The updated configurations are consistent with the physical meaning of the elements of the coherency matrix. Although the diameter of the dipole used in the experiment is very small, the superposition of two dipoles in the same plane will cause one of the dipoles to have a distance from the plane. Since the distance between one of the dipoles and plane cannot be ignored, it will cause an error in the scattering matrix obtained via the experiment. Due to the dipole alignment constrain, in the M7SD, two dipoles are placed in two planes, respectively, with a distance of half wavelength, which overcomes the drawback of the 7SD. The performance of the proposed method are demonstrated using the spaceborne C-band Gaofen-3 (GF-3) data, C-band Radarsat-2 data, and airborne L-band Experimental SAR (ESAR) data.

II. MODEL-BASED SCATTERING MATRIX

Within a radar range, if a single target exists, the scattering matrix is uniquely determined by the point target; if there are multiple targets within a radar range, the compound matrix is composed of scattering matrices of multiple targets [30]. If the distance between two or more targets is less than the radar range resolution, the compound matrix composed of multiple targets in the range resolution can be expressed as a weighted sum of multiple scattering matrices. A compound matrix consisting of two targets of distance d within a resolution unit can be expressed as

$$[S]^{\text{total}} = [S]_1 + [S]_2 P(d) \quad (1)$$

where $P(d) = \exp(-j\frac{4\pi d}{\lambda})$ denotes the phase delay caused by the spatial distance d . Suppose there are two targets in the radar range, $[S]_1$ and $[S]_2$ are the scattering matrices of target 1 and target 2, respectively. When d is 0, $\lambda/8$, $\lambda/4$, $3\lambda/8$, and $\lambda/2$, $P(d)$ are

$$\begin{aligned} P(0) &= 1, P(\lambda/8) = -j, P(\lambda/4) = -1 \\ P(3\lambda/8) &= j, P(\lambda/2) = 1. \end{aligned} \quad (2)$$

PolSAR acquires the polarimetric scattering matrix of each pixel in the scene by transmitting and receiving electromagnetic waves of different polarization modes, so as to analyze the target scattering characteristics. The general form of the radar scattering matrix is

$$[S] = \begin{bmatrix} S_{HH} & S_{HV} \\ S_{VH} & S_{VV} \end{bmatrix} = \begin{bmatrix} a & c \\ c & b \end{bmatrix} \quad (3)$$

where S_{HH} , S_{HV} , S_{VH} , and S_{VV} are the complex elements of the scattering matrix. $S_{HV} = S_{VH} = c$, which is consistent with the reciprocity assumption. S_{HV} is the backscattered return from vertical transmitting and horizontal receiving polarization.

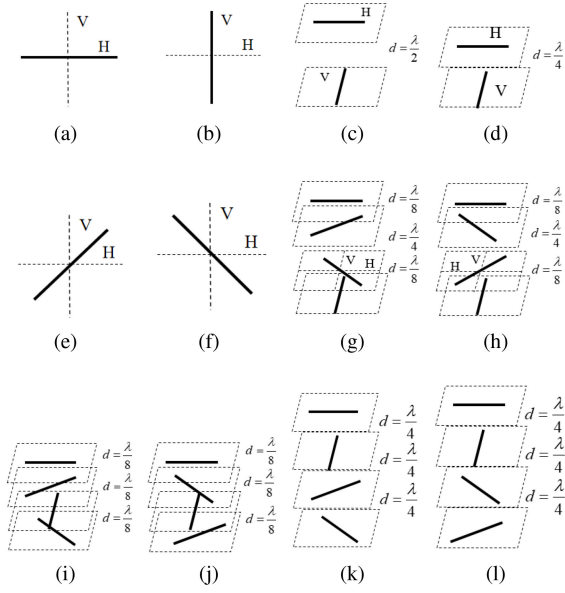


Fig. 1. Configurations for compounded scattering matrices. (a) Horizontal dipole. (b) Vertical dipole. (c) Dihedral. (d) Flat plate. (e) 45° oriented dipole. (f) -45° oriented dipole. (g) Right helix. (h) Left helix. (i) -45° Compound oriented dipoles (oriented quarter-wave reflector). (j) Compound oriented dipoles (45° oriented quarter-wave reflector). (k) 45° mixed dipoles. (l) -45° mixed dipoles.

For the case of monostatic backscattering, independent and identically distributed samples are averaged to form the coherency matrix, namely, $\langle [T] \rangle$, which can be expressed as

$$\begin{aligned} \langle [T] \rangle &= \langle k_p k_p^H \rangle = \begin{bmatrix} T_{11} & T_{12} & T_{13} \\ T_{21} & T_{22} & T_{23} \\ T_{31} & T_{32} & T_{33} \end{bmatrix} \\ &= \begin{bmatrix} \langle |k_1|^2 \rangle & \langle k_1 k_2^* \rangle & \langle k_1 k_3^* \rangle \\ \langle k_2 k_1^* \rangle & \langle |k_2|^2 \rangle & \langle k_2 k_3^* \rangle \\ \langle k_3 k_1^* \rangle & \langle k_3 k_2^* \rangle & \langle |k_3|^2 \rangle \end{bmatrix} \end{aligned} \quad (4)$$

where

$$k_p = \begin{bmatrix} k_1 \\ k_2 \\ k_3 \end{bmatrix} = \frac{1}{\sqrt{2}} \begin{bmatrix} S_{HH} + S_{VV} \\ S_{HH} - S_{VV} \\ 2S_{HV} \end{bmatrix} \quad (5)$$

In (4) and (5), k_p denotes the Pauli scattering vector.

Some models of compound scattering matrices derived from dipoles and their coherency matrices are shown in Fig. 1.

A. Configurations of Horizontal Dipole and Vertical Dipole

According to the 6SD, the dipole backscatters the electric field component to a direction parallel to the orientation angle with a strong polarization effect. The models of the horizontal dipole and vertical dipole are the same as models derived in [22], as shown in Fig. 1(a) and (b), respectively.

B. Configurations of Oriented Dipoles ($\pm 45^\circ$)

The configurations of the 45° oriented quarter-wave reflector and the -45° oriented quarter-wave reflector are shown in Fig. 1(e) and (f), respectively.

According to the 6SD, the 45° oriented quarter-wave reflector and the -45° oriented quarter-wave reflector can be used to characterize the real part of T_{13} , and the corresponding coherency matrices are, respectively, expressed as [22]

$$\begin{aligned} [T]_{\text{dipole}}^{45^\circ} &= \frac{1}{2} \begin{bmatrix} 1 & 0 & 1 \\ 0 & 0 & 0 \\ 1 & 0 & 1 \end{bmatrix} \\ [T]_{\text{dipole}}^{-45^\circ} &= \frac{1}{2} \begin{bmatrix} 1 & 0 & -1 \\ 0 & 0 & 0 \\ -1 & 0 & 1 \end{bmatrix}. \end{aligned} \quad (6)$$

C. Configurations of Compound Dipoles

Four dipoles (0° , 45° , -45° , 90°) are used to obtain the compound scattering matrices, as shown in Fig. 1(g) and (h), respectively. In both structures, there is an offset distance of $\lambda/2$ between the horizontal dipole and the vertical dipole. The two dipoles spaced apart by $\lambda/2$ can be used to characterize the configuration of the surface scattering element and reduce the unnecessary errors due to the superposition of dipoles in the same plane. Since the T_{13} element can be regarded as a coupling term between the first and third Pauli scattering vectors, these two configurations are consistent with the actual physical meaning.

Configurations of the compounded matrices can be expressed as

$$\begin{aligned} [S]_{\text{cd1}}^{\text{total}} &= [S]_{\text{dipole}}^H + [S]_{\text{dipole}}^V P(0) + [S]_{\text{dipole}}^{45^\circ} P\left(\frac{\lambda}{8}\right) \\ &+ [S]_{\text{dipole}}^{-45^\circ} P\left(\frac{3\lambda}{8}\right) = \begin{bmatrix} 1 & -j \\ -j & 1 \end{bmatrix} \\ [S]_{\text{cd2}}^{\text{total}} &= [S]_{\text{dipole}}^H + [S]_{\text{dipole}}^V P(0) + [S]_{\text{dipole}}^{-45^\circ} P\left(\frac{\lambda}{8}\right) \\ &+ [S]_{\text{dipole}}^{45^\circ} P\left(\frac{3\lambda}{8}\right) = \begin{bmatrix} 1 & j \\ j & 1 \end{bmatrix} \end{aligned} \quad (7)$$

where $[S]_{\text{dipole}}^H$ and $[S]_{\text{dipole}}^V$ are the scattering matrices of horizontal and vertical dipoles, respectively, and $[S]_{\text{dipole}}^{45^\circ}$ and $[S]_{\text{dipole}}^{-45^\circ}$ are the scattering matrices of 45° oriented quarter-wave reflector and -45° oriented quarter-wave reflector, respectively.

The corresponding coherency matrices can be written as

$$\begin{aligned} [T]_{\text{cd}}^{45^\circ} &= \frac{1}{2} \begin{bmatrix} 1 & 0 & -j \\ 0 & 0 & 0 \\ j & 0 & 1 \end{bmatrix} \\ [T]_{\text{cd}}^{-45^\circ} &= \frac{1}{2} \begin{bmatrix} 1 & 0 & j \\ 0 & 0 & 0 \\ -j & 0 & 1 \end{bmatrix}. \end{aligned} \quad (8)$$

According to the aforementioned equations, it can be confirmed that the oriented quarter-wave can be produced using

multiple composite-oriented dipoles. It is very important in the interpretation of the PolSAR coherency matrix, because the branches or leaves of vegetation are related to the mixture of dipole targets.

D. Configuration of the Helix Scattering Matrix (Imaginary Part of T_{23})

Helix scattering power, which is equivalent to the circular polarization power, appears in urban, vegetation, and mountainous area. In addition, it considers the nonreflection symmetry condition. Similar to the 6SD, as shown in Fig. 1(i) and (j), the corresponding left and right helix coherency matrices can be expressed as

$$\begin{aligned} [\mathbf{T}]_c^{\text{right}} &= \frac{1}{2} \begin{bmatrix} 0 & 0 & 0 \\ 0 & 1 & j \\ 0 & -j & 1 \end{bmatrix} \\ [\mathbf{T}]_c^{\text{left}} &= \frac{1}{2} \begin{bmatrix} 0 & 0 & 0 \\ 0 & 1 & -j \\ 0 & j & 1 \end{bmatrix}. \end{aligned} \quad (9)$$

E. Configurations of the Mixed Dipoles (Real Part of T_{23})

In the method proposed in this article, the configurations of the mixed dipoles used to obtain the real part of T_{23} are different from the configurations of the mixed compound scattering matrices used in the 7SD, as shown in Fig. 1(k) and (l), respectively. Four dipoles (0° , 45° , -45° , 90°) are arranged to form the compound scattering matrices with a distance of $\lambda/4$ between the planes of each two dipoles. With this configurations of the compound scattering matrices, the same results as the 7SD can be obtained. The configurations of the compound scattering matrices proposed in this article can be used as an appropriate approach.

The compound scattering matrices can be written as

$$\begin{aligned} [S]_{\text{hr1}}^{\text{total}} &= [S]_{\text{dipole}}^{\text{H}} + [S]_{\text{dipole}}^{\text{V}} P\left(\frac{\lambda}{4}\right) + [S]_1 P\left(\frac{\lambda}{2}\right) \\ &+ [S]_2 P\left(\frac{3\lambda}{4}\right) = \begin{bmatrix} 1 & 1 \\ 1 & -1 \end{bmatrix} \\ [S]_{\text{hr2}}^{\text{total}} &= [S]_{\text{dipole}}^{\text{H}} + [S]_{\text{dipole}}^{\text{V}} P\left(\frac{\lambda}{4}\right) + [S]_2 P\left(\frac{\lambda}{2}\right) \\ &+ [S]_1 P\left(\frac{3\lambda}{4}\right) = \begin{bmatrix} 1 & -1 \\ -1 & -1 \end{bmatrix}. \end{aligned} \quad (10)$$

The corresponding coherency matrices of the real part of T_{23} can be expressed as

$$\begin{aligned} [\mathbf{T}]_{\text{hr1}} &= \frac{1}{2} \begin{bmatrix} 0 & 0 & 0 \\ 0 & 1 & 1 \\ 0 & 1 & 1 \end{bmatrix} \\ [\mathbf{T}]_{\text{hr2}} &= \frac{1}{2} \begin{bmatrix} 0 & 0 & 0 \\ 0 & 1 & -1 \\ 0 & -1 & 1 \end{bmatrix}. \end{aligned} \quad (11)$$

In the experiment, some errors in the elements of the measured scattering matrix come from the multiple scattering of the

dipoles due to multiple scattering or mutual coupling effects. In the M7SD, by placing dipoles in different planes, the interpretation based on the elementary target scattering phenomena can be recognized.

III. REFINED VOLUME SCATTERING MODELS

In this article, different from the traditional decomposition methods, refined volume scattering models are proposed to better characterize the volume scattering elements of the coherency matrix. The mathematical forms of the coherency elements can be derived as [18], [31]

$$\begin{aligned} T_{11} &= (G_1 + G_3 + G_3^* + G_6) / 2 \\ T_{12} &= (G_1 - G_3 + G_3^* - G_6) / 2 \\ T_{13} &= G_2 + G_5^* \\ T_{22} &= (G_1 - G_3 - G_3^* + G_6) / 2 \\ T_{23} &= G_2 - G_5^* \\ T_{33} &= G_4 \end{aligned} \quad (12)$$

where

$$\begin{aligned} G_1 &= |a|^2 I_1 + |b|^2 I_2 + |c|^2 I_3 + 2\text{Re}(ab^*) I_4 \\ &+ 2\text{Re}(ac^*) I_5 + 2\text{Re}(bc^*) I_6 \\ G_2 &= a \frac{b^* - a^*}{2} I_5 + b \frac{b^* - a^*}{2} I_6 + c \frac{b^* - a^*}{2} I_3 \\ &+ ac^* I_{10} + bc^* I_9 + |c|^2 I_8 \\ G_3 &= (|a|^2 + |b|^2) I_4 - |c|^2 I_3 + ab^* I_1 + a^* b I_2 \\ &+ (b^* c - ac^*) I_5 + (a^* c - bc^*) I_6 \\ G_4 &= |a|^2 I_2 + |b|^2 I_1 + |c|^2 I_3 + 2\text{Re}(ab^*) I_4 \\ &- 2\text{Re}(ac^*) I_6 - 2\text{Re}(bc^*) I_5 \\ G_5 &= a^* \frac{b - a}{2} I_6 + b^* \frac{b - a}{2} I_5 - c^* \frac{b - a}{2} I_3 \\ &+ ca^* I_9 + b^* c I_{10} - |c|^2 I_8 \\ G_6 &= \frac{1}{4} |b - a|^2 I_3 + |c|^2 I_7 + \text{Re}\{c^*(b - a)\} I_8 \end{aligned} \quad (13)$$

and

$$\begin{aligned} I_1 &= \int_0^{2\pi} \cos^4 \theta p(\theta) d\theta, I_2 = \int_0^{2\pi} \sin^4 \theta p(\theta) d\theta \\ I_3 &= \int_0^{2\pi} \sin^2 2\theta p(\theta) d\theta, I_4 = \int_0^{2\pi} \sin^2 \theta \cos^2 \theta p(\theta) d\theta \\ I_5 &= \int_0^{2\pi} \cos^2 \theta \sin 2\theta p(\theta) d\theta, I_6 = \int_0^{2\pi} \sin^2 \theta \sin 2\theta p(\theta) d\theta \\ I_7 &= \int_0^{2\pi} \cos^2 2\theta p(\theta) d\theta, I_8 = \int_0^{2\pi} \sin 2\theta \cos 2\theta p(\theta) d\theta \\ I_9 &= \int_0^{2\pi} \sin^2 \theta \cos 2\theta p(\theta) d\theta, I_{10} = \int_0^{2\pi} \cos^2 \theta \cos 2\theta p(\theta) d\theta. \end{aligned} \quad (14)$$

Similar to the traditional four-component decomposition method, according to the generation of the cross-pol HV term, four volume scattering models in [32] are divided into the following two parts: the volume scattering generated by the vegetation and the volume scattering generated by the oriented dihedral scattering. For the volume scattering component generated by vegetation, according to the ratio of $|S_{HH}|^2$ to $|S_{VV}|^2$, one of the distributions is selected: uniform scattering, sinusoidal distribution, and cosine distribution.

A. Uniform Distribution

Similar to the traditional four-component decomposition method, the probability density function is $p(\theta) = \frac{1}{2\pi}$, and the corresponding coherency matrix can be written as

$$\langle[\mathbf{T}]_v^1\rangle = \frac{1}{4} \begin{bmatrix} 2 & 0 & 0 \\ 0 & 1 & 0 \\ 0 & 0 & 1 \end{bmatrix}. \quad (15)$$

B. Sinusoidal Distribution

For the volume scattering model subject to a sinusoidal distribution, the probability density function is modified as $p(\theta) = \frac{1}{2} \sin(\theta - \theta_d)$, for $\theta_d < \theta < \pi + \theta_d$, with $\int_{\theta_d}^{\pi+\theta_d} p(\theta) d\theta = 1$.

The angle θ in the distribution is taken from the horizontal axis seen from the radar and θ_d denotes the orientation angle, which can be expressed as

$$\theta_d = \frac{1}{4} \tan^{-1} \left(\frac{2\text{Re}(T_{23})}{T_{22} - T_{33}} \right). \quad (16)$$

According to the integral equation defined in the four-component decomposition proposed by Yamaguchi *et al.* [18], the results are derived as

$$\begin{aligned} I_1 &= \frac{3}{8} - \frac{1}{6} \cos 2\theta_d - \frac{1}{120} \cos 4\theta_d \\ I_2 &= \frac{3}{8} + \frac{1}{6} \cos 2\theta_d - \frac{1}{120} \cos 4\theta_d \\ I_3 &= \frac{1}{2} + \frac{1}{30} \cos 4\theta_d, I_4 = \frac{1}{8} + \frac{1}{120} \cos 4\theta_d \\ I_5 &= \frac{1}{3} \sin 2\theta_d + \frac{1}{15} \sin 4\theta_d, I_6 = \frac{1}{3} \sin 2\theta_d - \frac{1}{15} \sin 4\theta_d \\ I_7 &= \frac{1}{2} - \frac{1}{30} \cos 4\theta_d, I_8 = \frac{2}{15} \sin 4\theta_d \\ I_9 &= -\frac{1}{4} - \frac{1}{6} \cos 2\theta_d + \frac{1}{60} \cos 4\theta_d \\ I_{10} &= \frac{1}{4} - \frac{1}{6} \cos 2\theta_d - \frac{1}{60} \cos 4\theta_d. \end{aligned} \quad (17)$$

When the sinusoidal distribution is selected, the volume scattering model is equal to a cloud of randomly oriented, very thin horizontal cylinder-like scatterers (the vertical dipole). According to the assumption of the reflection symmetry, the T_{13} and T_{23} elements are forced to zero and the volume scattering averaged

coherency matrix $\langle[\mathbf{T}]_v^2\rangle$ can be written as

$$\langle[\mathbf{T}]_v^2\rangle = \begin{bmatrix} \frac{1}{2} & \frac{\cos 2\theta_d}{6} & 0 \\ \frac{\cos 2\theta_d}{6} & \frac{15 - \cos 4\theta_d}{60} & 0 \\ 0 & 0 & \frac{15 + \cos 4\theta_d}{60} \end{bmatrix}. \quad (18)$$

C. Cosine Distribution

In this case, the probability density function can be expressed as $p(\theta) = \frac{1}{2} \cos(\theta - \theta_d)$, for $\theta_d < \theta < \pi + \theta_d$, with $\int_{\theta_d}^{\pi+\theta_d} p(\theta) d\theta = 1$.

Similar to the sinusoidal contribution, the elements of the volume scattering model have similar representations. When the cosine distribution is selected, the volume scattering model is equal to a cloud of randomly oriented, very thin vertical cylinder-like scatterers (the horizontal dipole), and the volume scattering averaged coherency matrix $\langle[\mathbf{T}]_v^3\rangle$ can be written as

$$\langle[\mathbf{T}]_v^3\rangle = \begin{bmatrix} \frac{1}{2} & -\frac{\cos 2\theta_d}{6} & 0 \\ -\frac{\cos 2\theta_d}{6} & \frac{15 - \cos 4\theta_d}{60} & 0 \\ 0 & 0 & \frac{15 + \cos 4\theta_d}{60} \end{bmatrix}. \quad (19)$$

D. Volume Scattering Caused by the Oriented Dihedral Scatterer

Since the HV term generated by the oriented building is different from the HV term generated by the vegetation, the performance in distinguishing buildings from vegetation areas is unacceptable with a uniform volume scattering model. In addition, the cross-pol power generated by the oriented building is different from the double-bounce scattering power. Therefore, the scattering components in urban areas cannot be fully represented by the double-bounce scattering model.

According to Sato *et al.* [32], to better characterize the performance of the orientation angles, the probability density function of the volume scattering caused by the oriented dihedral scatterers are modified as $p(\theta) = \frac{1}{2} \cos(\theta - \theta_d)$, for $\theta_d < \theta < \pi + \theta_d$, with $\int_{\theta_d}^{\pi+\theta_d} p(\theta) d\theta = 1$. According to the coherency matrix of rotated dihedral elementary scatterers with an orientation angle of θ , namely, $T_d(\theta)$, and the refined probability density function, the coherency matrix elements of the volume scattering can be obtained

$$\begin{aligned} \langle[\mathbf{T}]_v^4\rangle &= \int_{\theta_d}^{\pi+\theta_d} T_d(\theta) p(\theta) d\theta \\ &= \begin{bmatrix} 0 & 0 & 0 \\ 0 & \frac{1}{2} - \frac{1}{30} \cos 4\theta_d & 0 \\ 0 & 0 & \frac{1}{2} + \frac{1}{30} \cos 4\theta_d \end{bmatrix} \end{aligned} \quad (20)$$

where

$$T_d(\theta) = \begin{bmatrix} 0 & 0 & 0 \\ 0 & \cos^2 2\theta & 0 \\ 0 & 0 & \sin^2 2\theta \end{bmatrix}. \quad (21)$$

IV. MODIFIED SEVEN-COMPONENT DECOMPOSITION METHOD

The rationality of the model-based decomposition results mainly depends on the selected volume scattering model, and different volume scattering models are arranged to characterize

various cross-polarization components. The coherency matrix can be divided into seven submatrices

$$\begin{aligned} \langle [\mathbf{T}] \rangle &= \frac{f_s}{1 + |\beta|^2} \begin{bmatrix} 1 & \beta^* & 0 \\ \beta & |\beta|^2 & 0 \\ 0 & 0 & 0 \end{bmatrix} + \frac{f_d}{1 + |\alpha|^2} \begin{bmatrix} |\alpha|^2 & \alpha & 0 \\ \alpha^* & 1 & 0 \\ 0 & 0 & 0 \end{bmatrix} \\ &+ \frac{f_c}{2} \begin{bmatrix} 0 & 0 & 0 \\ 0 & 1 & \pm j \\ 0 & \mp j & 1 \end{bmatrix} + \frac{f_{hr}}{2} \begin{bmatrix} 0 & 0 & 0 \\ 0 & 1 & \pm 1 \\ 0 & \pm 1 & 1 \end{bmatrix} \\ &+ \frac{f_{cd}}{2} \begin{bmatrix} 1 & 0 & \pm j \\ 0 & 0 & 0 \\ \mp j & 0 & 1 \end{bmatrix} + \frac{f_{od}}{2} \begin{bmatrix} 1 & 0 & \pm 1 \\ 0 & 0 & 0 \\ \pm 1 & 0 & 1 \end{bmatrix} \\ &+ f_v \langle [\mathbf{T}] \rangle_v^i, \quad i = 1, 2, 3, 4. \end{aligned} \quad (22)$$

Different values of i correspond to different volume scattering models defined in (18), (21), (22), and (23).

A. Solution of (25) With Sinusoidal Distribution

In this case, the element relations can be written as

$$\begin{aligned} T_{11} &= f_s + f_d |\alpha|^2 + \frac{f_v}{2} + \frac{f_{od}}{2} + \frac{f_{cd}}{2} \\ T_{12} &= f_s \beta^* + f_d \alpha + \frac{f_v \cos 2\theta_d}{6} \\ T_{13} &= \pm \frac{f_{od}}{2} \pm j \frac{f_{cd}}{2} \\ T_{22} &= f_s |\beta|^2 + f_d + \frac{f_c}{2} + \frac{f_{hr}}{2} + \frac{(15 - \cos 4\theta_d) f_v}{60} \\ T_{23} &= \pm \frac{f_{hr}}{2} \pm j \frac{f_c}{2} \\ T_{33} &= \frac{(15 + \cos 4\theta_d) f_v}{60} + \frac{f_{cd}}{2} + \frac{f_{od}}{2} + \frac{f_c}{2} + \frac{f_{hr}}{2}. \end{aligned} \quad (23)$$

According to the aforementioned equations, the elements f_v , f_c , f_{hr} , f_{cd} , and f_{od} can be derived and a set of three equations to obtain the four remaining unknowns (α , β , f_s , f_d) can be found:

$$\begin{aligned} f_c &= 2 |\operatorname{Im}(T_{23})|, \quad f_{hr} = 2 |\operatorname{Re}(T_{23})| \\ f_{cd} &= 2 |\operatorname{Im}(T_{13})|, \quad f_{od} = 2 |\operatorname{Re}(T_{13})| \\ f_v &= \frac{30}{15 + \cos 4\theta_d} (2T_{33} - f_c - f_{hr} - f_{od} - f_{cd}) \\ S &= f_s + f_d |\alpha|^2 = T_{11} - \frac{f_v}{2} - \frac{f_{od}}{2} - \frac{f_{cd}}{2} \\ C &= f_s \beta^* + f_d \alpha = T_{12} - \frac{f_v \cos 2\theta_d}{6} \\ D &= f_s |\beta|^2 + f_d = T_{22} - \frac{f_c}{2} - \frac{f_{hr}}{2} - \frac{(15 - \cos 4\theta_d) f_v}{60}. \end{aligned} \quad (24)$$

B. Solution of (25) With Uniform Distribution

Similar to (27), after the expansion and rearrangement, the coefficients and their relationships can be expressed as

$$\begin{aligned} f_c &= 2 |\operatorname{Im}(T_{23})|, \quad f_{hr} = 2 |\operatorname{Re}(T_{23})| \\ f_{cd} &= 2 |\operatorname{Im}(T_{13})|, \quad f_{od} = 2 |\operatorname{Re}(T_{13})| \\ f_v &= 2 (2T_{33} - f_c - f_{hr} - f_{od} - f_{cd}) \\ S &= f_s + f_d |\alpha|^2 = T_{11} - \frac{f_v}{2} - \frac{f_{od}}{2} - \frac{f_{cd}}{2} \\ C &= f_s \beta^* + f_d \alpha = T_{12} \\ D &= f_s |\beta|^2 + f_d = T_{22} - \frac{f_c}{2} - \frac{f_{hr}}{2} - \frac{f_v}{4}. \end{aligned} \quad (25)$$

C. Solution of (25) With Cosine Distribution

In this case, the coefficients and their relationships can be expressed as

$$\begin{aligned} f_c &= 2 |\operatorname{Im}(T_{23})|, \quad f_{hr} = 2 |\operatorname{Re}(T_{23})| \\ f_{cd} &= 2 |\operatorname{Im}(T_{13})|, \quad f_{od} = 2 |\operatorname{Re}(T_{13})| \\ f_v &= \frac{30}{15 + \cos 4\theta_d} (2T_{33} - f_c - f_{hr} - f_{od} - f_{cd}) \\ S &= f_s + f_d |\alpha|^2 = T_{11} - \frac{f_v}{2} - \frac{f_{od}}{2} - \frac{f_{cd}}{2} \\ C &= f_s \beta^* + f_d \alpha = T_{12} + \frac{f_v \cos 2\theta_d}{6} \\ D &= f_s |\beta|^2 + f_d = T_{22} - \frac{f_c}{2} - \frac{f_{hr}}{2} - \frac{(15 - \cos 4\theta_d) f_v}{60}. \end{aligned} \quad (26)$$

D. Solution of (25) With the Volume Scattering Caused by the Oriented Dihedral Scatter

The coefficients and their relationships can be expressed as

$$\begin{aligned} f_c &= 2 |\operatorname{Im}(T_{23})|, \quad f_{hr} = 2 |\operatorname{Re}(T_{23})| \\ f_{cd} &= 2 |\operatorname{Im}(T_{13})|, \quad f_{od} = 2 |\operatorname{Re}(T_{13})| \\ f_v &= \frac{15}{15 + \cos 4\theta_d} (2T_{33} - f_c - f_{hr} - f_{od} - f_{cd}) \\ S &= f_s + f_d |\alpha|^2 = T_{11} - \frac{f_{od}}{2} - \frac{f_{cd}}{2} \\ C &= f_s \beta^* + f_d \alpha = T_{12} \\ D &= f_s |\beta|^2 + f_d = T_{22} - \frac{f_c}{2} - \frac{f_{hr}}{2} - \frac{(15 - \cos 4\theta_d) f_v}{30}. \end{aligned} \quad (27)$$

From the volume scattering models obtained by the aforementioned new probability distributions, it can be seen that when $\theta_d = 0$, the previously described volume scattering models are the same as the volume scattering models in the extend four-component decomposition method proposed by Sato *et al.*

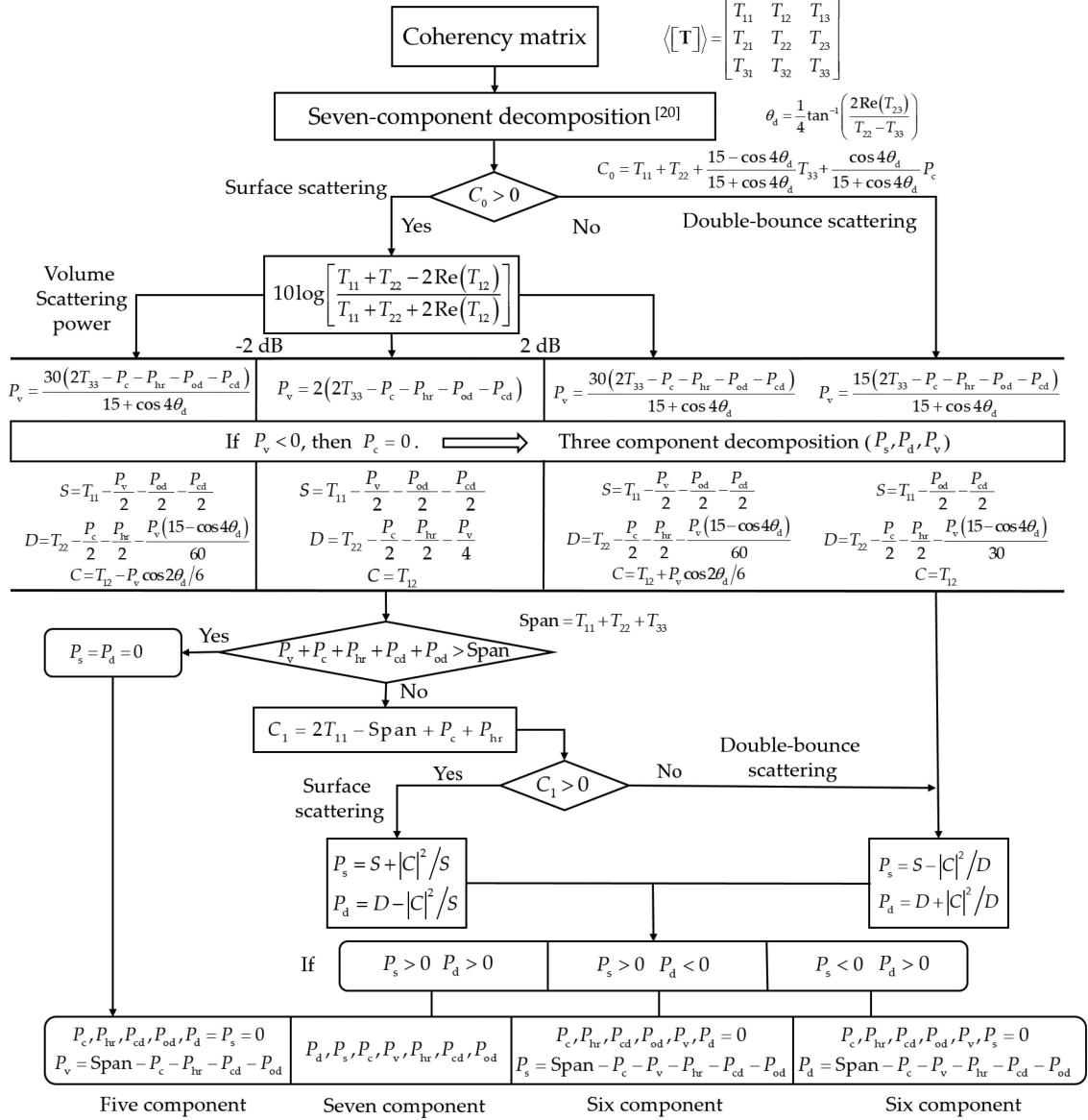


Fig. 2. Flowchart of the proposed decomposition method.

[32]. Moreover, when $\theta_d \neq 0$, the volume scattering models are related to the orientation angles and can be used to characterize the volume scattering components with various orientation angles. These refined volume scattering models are used to describe the volume scattering powers of targets with various orientation angles and the OVS can be effectively overcome.

The flowchart of the proposed method is shown in Fig. 2.

E. Branch Condition

It is necessary to solve (27)–(30) by making assumptions in advance to reduce the number of unknowns. Similar to the equations derived in [29], the dominant scattering mechanism (the double-bounce scattering or the surface scattering) of the matrix depends on the value of $\text{Re}\{\langle S_{HH}S_{VV}^* \rangle\}$ [17]. The nondihedral scattering of vegetation makes $\text{Re}\{\langle S_{HH}S_{VV}^* \rangle\}$ positive,

whereas the dihedral scattering of oriented buildings makes $\text{Re}\{\langle S_{HH}S_{VV}^* \rangle\}$ negative. To this reason, two branch conditions are used to determine the sign of $\text{Re}\{\langle S_{HH}S_{VV}^* \rangle\}$

According to the volume scattering model caused by the oriented buildings, the equation of $\text{Re}\{\langle S_{HH}S_{VV}^* \rangle\}$ can be rearranged to determine the dominant scattering characteristic, which can be written as

$$\begin{aligned} \text{Re}\{\langle S_{HH}S_{VV}^* \rangle\} &= \text{Re}\{f_s\beta^* + f_d\alpha\} \\ &= \frac{15 - \cos 4\theta_d}{60} f_v - \frac{1}{4} f_c - \frac{1}{4} f_{hr} + \frac{1}{4} f_{cd} + \frac{1}{4} f_{od} \\ C_0 &= 2\text{Re}\{f_s\beta^* + f_d\alpha\} = T_{11} - T_{22} \\ &+ \frac{15 - \cos 4\theta_d}{30} f_v + \frac{1}{2} (f_c + f_{hr}) - \frac{1}{2} (f_{od} + f_{cd}). \quad (28) \end{aligned}$$

If $C_0 > 0$, the volume scattering power is assigned to surface scattering, which is generated by the vegetation areas; if $C_0 \leq 0$, the volume scattering power is assigned to double-bounce scattering, which is generated by the oriented building areas.

Similarly, after the suitable volume scattering model is selected, another relation can be derived to determine the dominant scattering (e.g., double-bounce scattering or surface scattering)

$$\begin{aligned} C_1 &= 2\text{Re}\{f_s\beta^* + f_d\alpha\} \\ &= T_{11} - T_{22} - T_{33} + f_c + f_{hr}. \end{aligned} \quad (29)$$

If $C_1 > 0$, surface scattering is the dominant mechanism. Since the double-bounce component is negligible, the value of α can be assumed to be equal to 0. In this condition, the solutions of the undetermined equations are

$$f_s = S, \beta^* = C S, f_d = D - |C|^2 S. \quad (30)$$

If $C_1 \leq 0$, double-bounce scattering is the dominant mechanism. Since the surface component is negligible, the value of $|\beta|$ can be assumed to be equal to 0. In this condition, the solutions of the undetermined equations are

$$f_d = D, \alpha = C D, f_s = S - |C|^2 D. \quad (31)$$

Once the coefficients are determined, the scattering powers can be expressed as

$$\begin{aligned} P_s &= f_s (1 + |\beta|^2), P_d = f_d (1 + |\alpha|^2) \\ P_v &= f_v, P_c = f_c, P_{hr} = f_{hr}, P_{od} = f_{od}, P_{cd} = f_{cd}. \end{aligned} \quad (32)$$

In addition, the scattering powers are equally applicable to the oriented dihedral scattering areas.

V. EXPERIMENTAL RESULTS

In this article, the experimental results are derived from the spaceborne C-band GF-3 data, C-band Radarsat-2 data, and airborne L-band ESAR data. Several polarimetric analysis techniques are employed to evaluate the performance of the proposed decomposition method.

A. Decomposition Results of the GF-3 Dataset

The study area of GF-3 image is located in San Francisco area, USA, with a size of 7684×5836 , and the image includes forests, ocean, and buildings with various orientation angles. The data were collected on September 15, 2017 and the acquisition mode is ascending. The corresponding incidence angle range varies from 19.86° to 22.59° , and the central coordinates are (37.6°N , 122.4°W). The spatial resolution of the data corresponds to $8\text{ m} \times 8\text{ m}$ (azimuth \times range) and the ensemble average is calculated with a factor of 9 in both the azimuth and range directions. A refined Lee filter has been applied to smooth the speckle effect using a 7×7 moving window. The optical image and the Pauli decomposition results of this study site are shown in Fig. 3, respectively.

In this subsection, the performance of the proposed decomposition method, namely, M7SD, is evaluated by qualitative

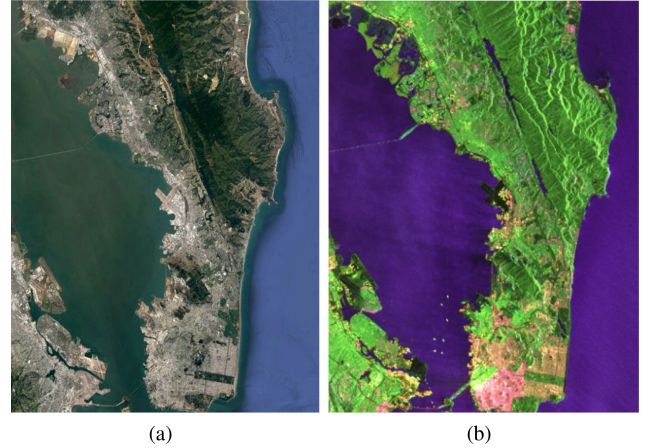


Fig. 3. C-band GF-3 data in San Francisco, USA. (a) Optical image from Google Earth. (b) Corresponding Pauli pseudocolor map (blue: $|HH + VV|$, red: $|HH - VV|$, and green: $2|HV|$).

and quantitative comparisons with the existing scattering power decompositions: the traditional three-component decomposition method (FDD) [17], the four-component decomposition method with rotation of coherency matrix (Y4R) [19], the general four-component decomposition method with unitary transformation of coherency matrix (G4U) [23], the six-component decomposition method (6SD) [22], and the seven-component decomposition method (7SD) [29].

The aforementioned six model-based decomposition methods are applied to the coherency matrix of the study site, and the color-coded FDD, Y4R, G4U, 6SD, 7SD, and M7SD decomposition results are shown in Fig. 4, respectively. In Fig. 4, the brightness of the color corresponds to the intensity. The volume scattering power mainly contributes to the vegetated areas and the dominant scattering mechanism of the ocean is surface scattering. As can be seen from Fig. 4, compared with the existing decomposition methods, the entire image becomes redder and the volume scattering is significantly reduced in the M7SD. In the decomposition results obtained via M7SD, the scattering mechanism of oriented and orthogonal building areas can be effectively interpreted and the volume scattering can be properly reduced.

To quantitatively evaluate the performance of the M7SD, four patches, including A (ocean), B (forest), C (orthogonal buildings), and D (oriented buildings) are selected as the regions of interest (ROI), as shown in Fig. 4(f). For the aforementioned six decomposition methods (including FDD, Y4R, G4U, 6SD, 7SD, and M7SD), the mean power statistics of the selected patches are shown in Fig. 5.

In the patches A and B, the dominant scattering mechanisms of the ocean and vegetated areas can be effectively identified, respectively. For the ocean, the dominant scattering mechanism is surface scattering, and the percentage contribution of the surface scattering is 84.3%, 85%, 85.2%, 89.1%, 88.7%, and 89% for FDD, Y4R, G4U, 6SD, 7SD, and M7SD, respectively. All of the aforementioned six methods can be used to characterize the scattering mechanism of the water body. For the

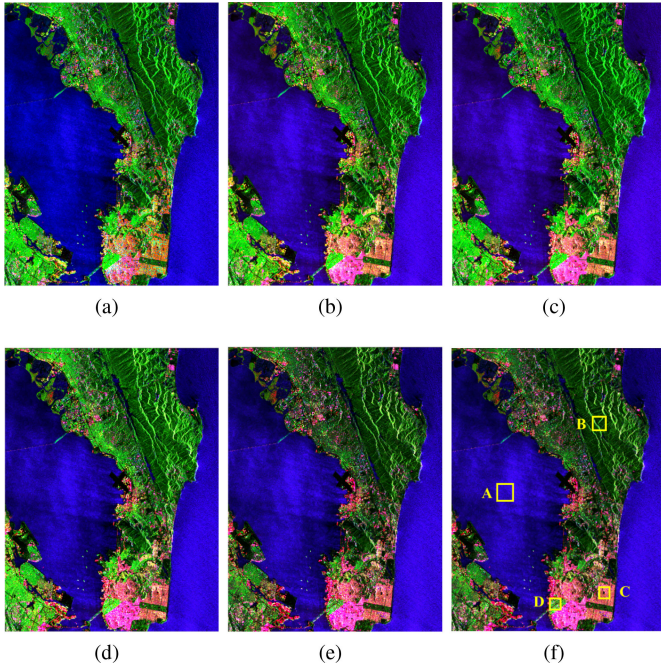


Fig. 4. Color-coded scattering power decomposition with red (double-bounce scattering), green (volume scattering), and blue (surface scattering). (a)–(f) Decomposition results using the FDD, Y4R, G4U, 6SD, 7SD, and M7SD, respectively.

vegetation area, the dominant scattering mechanism is volume scattering, and the statistics demonstrate 87.5%, 77.4%, 74.7%, 52.6%, 44.7%, and 44.9% of volume scattering in FDD, Y4R, G4U, 6SD, 7SD, and M7SD, respectively. In addition, for 6SD, the compound scattering power components (P_{od} and P_{cd}) are obtained, and a part of the volume scattering power is included in these compound scattering components. Similarly, 7SD and M7SD increase the compound scattering power, namely, P_{hr} , and the volume scattering component is not only included in the compound scattering components generated by T_{23} , but also in the compound scattering component generated by term T_{13} . According to aforementioned analysis, the aforementioned six decomposition methods can reasonably interpret the scattering mechanisms of the vegetated areas and the water body.

For the orthogonal building area (patch C), the dominant mechanism is double-bounce scattering, which is predominantly observed in all previously described decomposition methods. The percentage contribution of double-bounce scattering power in patch C is 56.5%, 56.8%, 57%, 57.1%, 54.7%, and 54.6% for FDD, Y4R, G4U, 6SD, 7SD, and M7SD, respectively. Since the cross-polar power makes a small contribution in the orthogonal structures, the percentage of P_{od} , P_{cd} , and P_{hr} is minimal.

In the building area with large orientation angles (patch D), the orientation angle of the buildings in the selected area are about 40° to the radar line of sight. According to the decomposition results obtained via the FDD, Y4R, and G4U, the dominant mechanism (double-bounce/surface scattering) of the buildings with large orientation angles is misinterpreted into volume scattering, resulting in the OVS. In Fig. 5, the contributions of the volume scattering power can be properly reduced via the 6SD

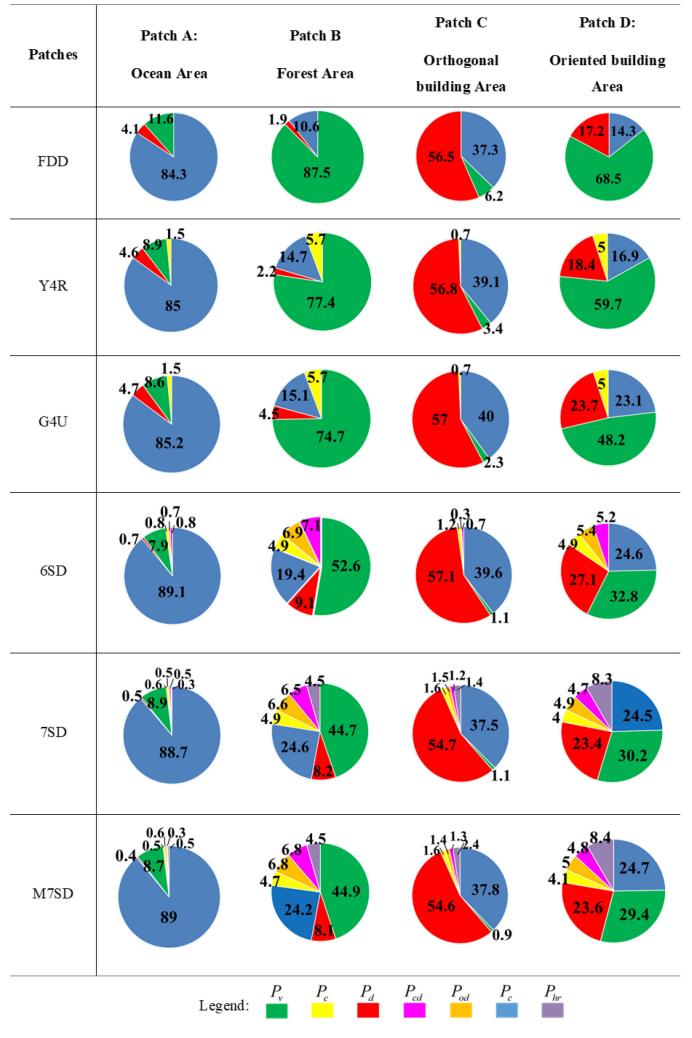


Fig. 5. Mean power statistics for the decompositions results (FDD, Y4R, G4U, 6SD, 7SD, and M7SD) of the selected patches in Fig. 4(f). The values are the percentage of the total power.

and 7SD and the OVS can be further overcome via the M7SD. For the oriented building area, the volume scattering for the M7SD is decreased from 68.5% (the result obtained by the FDD) to 29.4%. Except for the 7SD, the decrease is mainly determined by the addition of the new scattering component (P_{hr}). Compared with the 7SD, the contribution of the volume scattering is reduced by 0.8% in the oriented building area. This decrease is caused by the employment of the refined volume scattering models. The contribution of the double-bounce scattering is increased from 17.2% in FDD to 23.6% in the M7SD, which demonstrates the potential of the M7SD in interpreting the scattering mechanism of the oriented buildings.

There is an interesting phenomenon that the contributions of double-bounce scattering in the M7SD and 7SD are lower than that obtained via the 6SD. This can be interpreted as: in the 6SD, prior to the decomposition, the OAC is performed and the coherency matrix is rotated to the radar line of sight. The real part of the T_{23} term is set to 0 and the double-bounce scattering component is derived from the rotated term T'_{22} [13], which is

TABLE I
PERCENTAGE OF PIXELS WITH NEGATIVE SCATTERING POWERS

Methods	FDD	Y4R	G4U	6SD	7SD	M7SD
Percentage of negative scattering powers (%)	38.97	32.11	26.43	20.92	20.06	19.70

maximized via the OAC. Since the coherency matrices of the 7SD and M7SD are not rotated, the double-bounce scattering component is only derived from the term T_{22} of the coherency matrix. In addition, the 7SD and M7SD increase a mixed dipoles scattering power (P_{hr}), which combines the oriented and nonoriented dipoles and also contributes to the compound scattering power. Therefore, in 7SD and M7SD, the contribution of double-bounce scattering is less than 6SD.

For model-based decomposition results, the occurrence of the negative scattering power is an important evaluation criterion to evaluate the performance of the method. The percentage of negative scattering power pixels obtained by the previously described six decomposition methods are listed in Table I. It can be seen from the table that as the decomposition method continues to extend and the scattering components become increasingly complex, the percentage of pixels with negative scattering powers decreases. For the M7SD, compared with the FDD, Y4R, G4U, 6SD and 7SD, the percentage of the pixels with negative scattering is reduced by 19.27%, 12.41%, 6.73%, 1.22%, and 0.36%, respectively. Although, compared with the 6SD and 7SD, the improvements in terms of reduced number of pixels characterized by negative powers is negligible by using the M7SD method in this image, it has the potential to reduce the amount of negative scattering elements for the large-size images.

B. Decomposition Results of the Building Areas

In this subsection, the Radarsat-2 data with a size of 14413×2820 are used to evaluate the performance of the decomposition results of urban areas. The image was acquired on April 9, 2008 and the spatial resolution of Radarsat-2 is 4.7 m in both range and azimuth directions. The window size was set as 9×3 , corresponding to 42.3 m by 14.1 m on the ground area. The acquisition mode is descending and the central coordinates are $(37.55^\circ\text{N}, 122.43^\circ\text{W})$. The optical image of the study site and the corresponding Pauli RGB image are shown in Fig. 6. The land covers contained in the study site are the same as that obtained by the GF-3 satellite. The pseudocolor maps of the decomposition results obtained via the previously described six decomposition methods (FDD, Y4R, G4U, 6SD, 7SD, and M7SD) are shown in Fig. 7.

To further evaluate the performance of the M7SD in the building areas, an ROI including buildings with various orientation angles, is selected, as shown in Fig. 7(f). The enlarged decomposition results of the study site obtained via the previously described decomposition methods and the corresponding optical image are shown in Fig. 8. Two oriented building areas (Patches I and II) and an orthogonal building area (patch III) are selected for

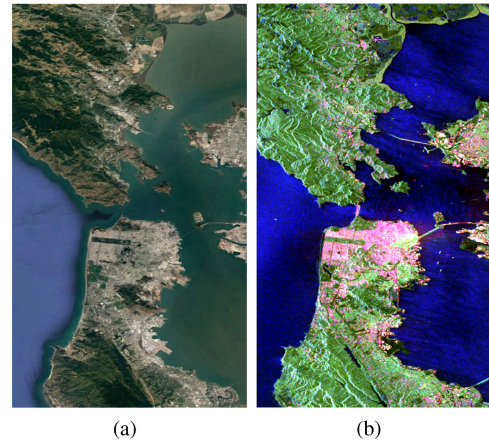


Fig. 6. Radarsat-2 data in San Francisco, USA. (a) Optical image from Google Earth. (b) Corresponding Pauli pseudocolor map (blue: $|HH + VV|$, red: $|HH - VV|$, and green: $2|HV|$).

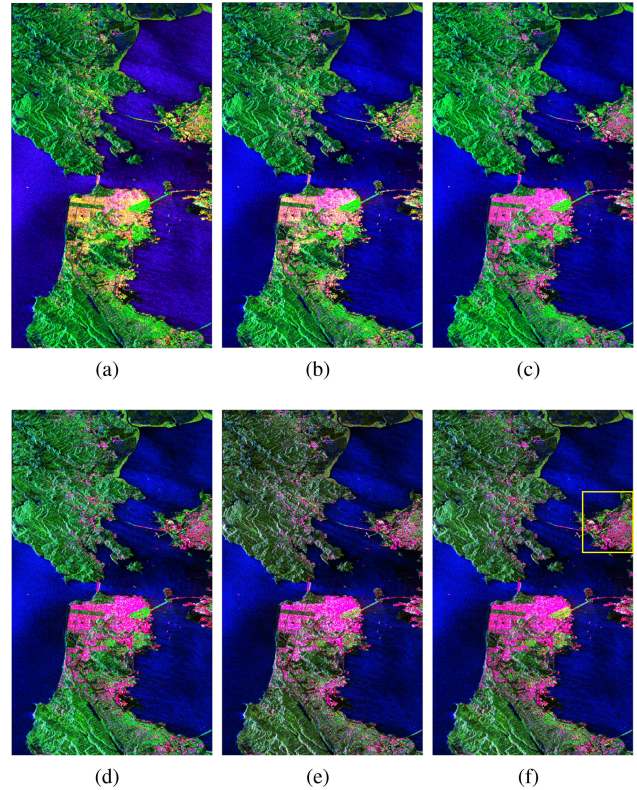


Fig. 7. Color-coded scattering power decomposition with red (double-bounce scattering), green (volume scattering), and blue (surface scattering). (a)–(f) Decomposition results using the FDD, Y4R, G4U, 6SD, 7SD, and M7SD, respectively.

comparative analysis, as shown in Fig. 8(a). It can be seen that, with the continuous development of the decomposition method, the decomposition results are more and more consistent with the actual terrain types, and the scattering mechanisms of various land covers can be appropriately interpreted. The histograms of the orientation angles for these patches are shown in Fig. 9. According to Figs. 8 and 9, for the orthogonal building areas, all the decomposition methods can correctly characterize the scattering mechanisms and the dominant scattering mechanism

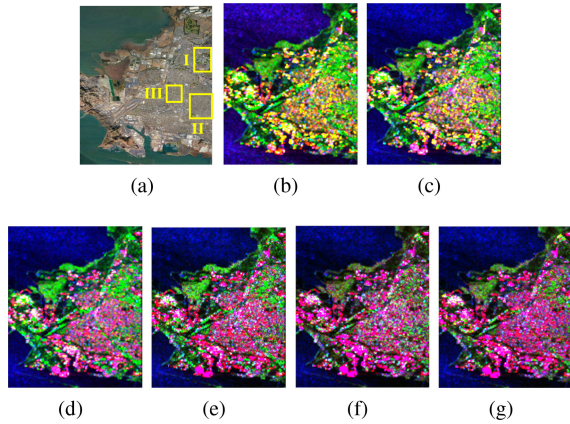


Fig. 8. Images of the yellow box areas in Fig. 7(f). (a) Optical image of the yellow box areas. (b)–(g) Corresponding decomposition results using the FDD, Y4R, G4U, 6SD, 7SD, and M7SD, respectively.

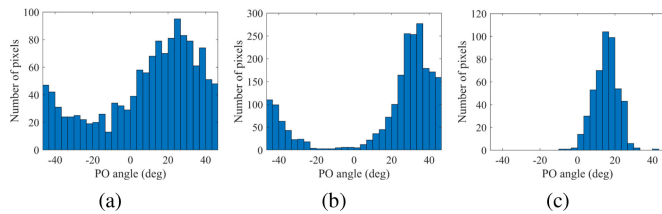


Fig. 9. Histograms of the selected patches I, II, and III, respectively.

is double-bounce scattering. However, for the oriented building areas, the decomposition results obtained via the M7SD have superior advantages in interpreting the scattering mechanisms.

To quantitatively evaluate the performance of the M7SD in the oriented building areas, the mean power statistical of the selected oriented building areas (patches I and II) are shown in Fig. 10. For patch I, compared with the existing five decomposition methods, the volume scattering is reduced by 61.4%, 58.3%, 36%, 9.8%, and 4.1% in the M7SD, respectively, and the double-bounce scattering obtained via the M7SD is effectively increased. Moreover, similar results can be obtained in patch II. The double-bounce scattering can be appropriately increased and the OVS can be overcome. Therefore, the scattering mechanism of the oriented building area can be effectively interpreted.

C. Airborne L-Band SAR Data

To verify the validity of the M7SD for SAR image decomposition results in different bands, the airborne L-band ESAR data obtained by the German Aerospace Center laboratory are selected. The study site is located in the Oberpfaffenhofen, Germany, with the size of 1300×1200 . As the equivalent number of looks of the data is high enough, no more averaging or filter is needed. The incidence angle is about 40° , and the geolocation center of is ($48^\circ 5' 3''N$, $11^\circ 17' 4''E$). The optical image and the corresponding Pauli RGB image are shown in Fig. 11.

In the aforementioned subsections, the M7SD has been compared to the five existing decomposition methods. Since both 7SD and M7SD divide the coherency matrix into seven scattering components, in this subsection, the M7SD is compared with the 7SD to demonstrate the performance of the refined volume

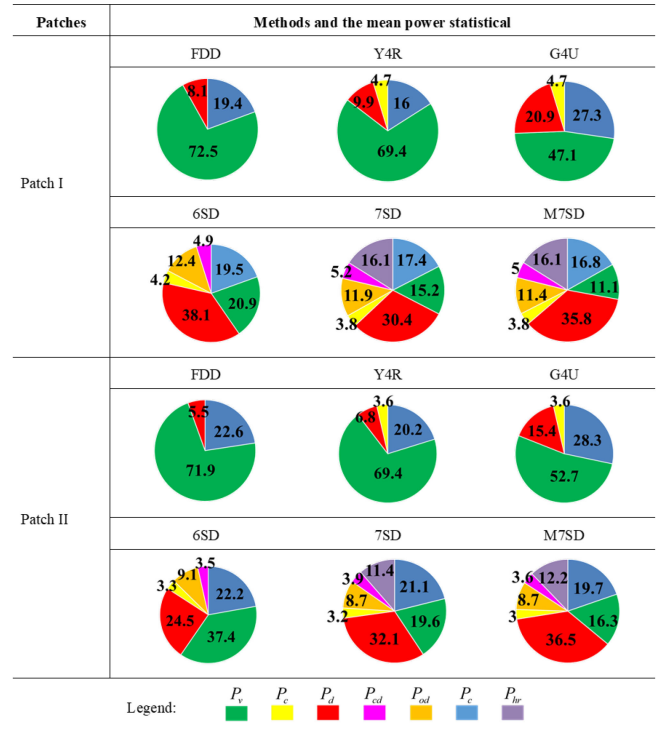


Fig. 10. Mean power statistics for the decompositions results (FDD, Y4R, G4U, 6SD, 7SD, and M7SD). The study sites (patches I and II) are highlighted by the yellow boxes in Fig. 8(a). The values are the percentage of the total power.

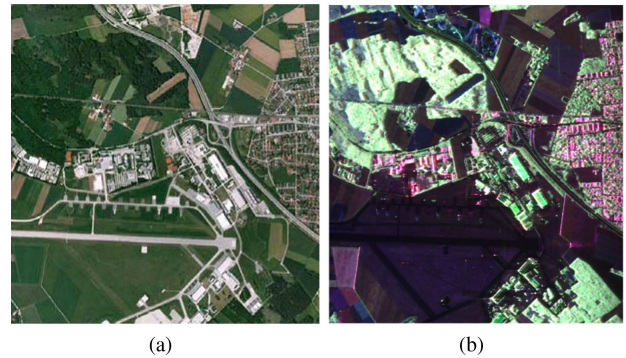


Fig. 11. L-band ESAR images of the study site over the Oberpfaffenhofen, German. (a) Optical image from Google Earth. (b) Corresponding Pauli pseudocolor map (blue: $|HH + VV|$, red: $|HH - VV|$, and green: $2|HV|$).

scattering models utilized in the M7SD. The decomposition results of the M7SD and 7SD are shown in Fig. 12(a) and (b), respectively.

It can be seen from Fig. 12(a) and (b) that, for the building areas parallel or approximately parallel to the flight direction (the right areas of the image), the decomposition result obtained via the 7SD is similar to that obtained via the M7SD. The scattering mechanism of these building areas can be reasonably characterized. To evaluate the performance of the 7SD and M7SD, two oriented building areas shown in Fig. 12(a) are selected as the study sites for further analysis. The enlarged decomposition results are shown in Fig. 12(c)–(f).

According to the optical images shown in Fig. 11(a), compared with the 7SD, the scattering mechanism of the oriented

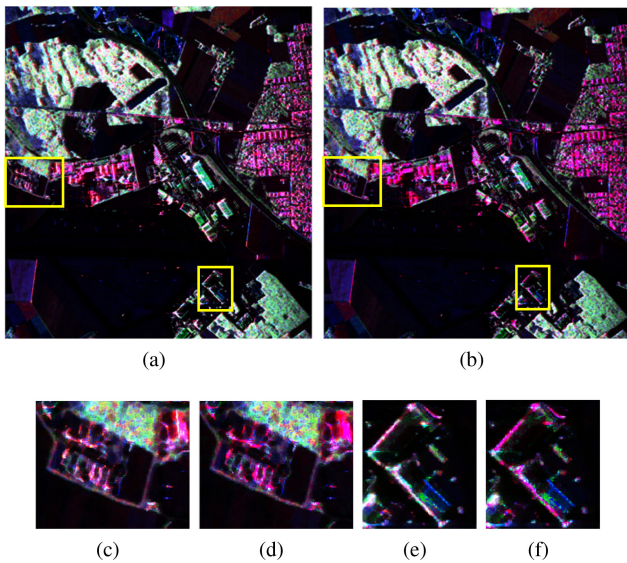


Fig. 12. Decomposition results using (a) 7SD and (b) M7SD. (c)–(f) Enlarged decomposition results of the selected patches [in Fig. 12(a)]. (c) and (e) Results obtained via the 7SD. (d) and (f) Results obtained via the M7SD.

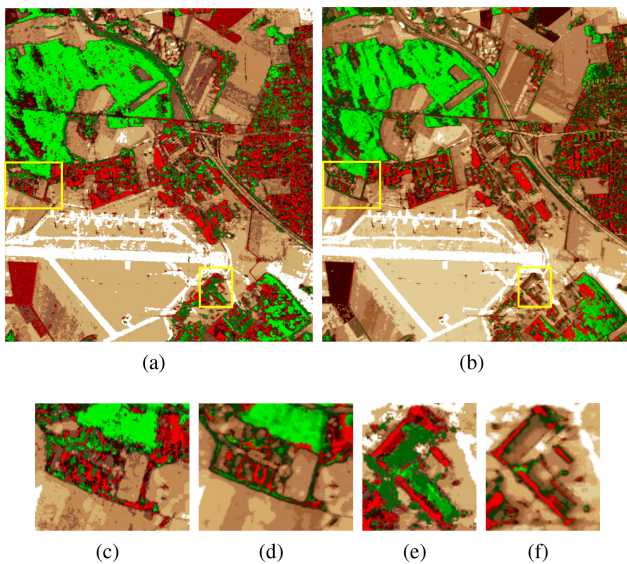


Fig. 13. Classification results using (a) 7SD and (b) M7SD. (c)–(f) Enlarged classification results of the selected patches [in Fig. 13(a)]. (c) and (e) Results obtained via the 7SD. (d) and (f) Results obtained via the M7SD.

building areas can be reasonably interpreted via the M7SD. The building area can be decomposed into red/pink. To more intuitively evaluate the rationality of the decomposition results of the study sites, the Wishart classification method [33] is carried out to show the classification results derived by the 7SD and M7SD, as shown in Fig. 13(a) and (b). The enlarged classification results of the selected patches are shown in Fig. 13(c)–(f). According to the classification results, compared with the 7SD, the volume scattering component is further reduced and the OVS can be effectively overcome. The dominant scattering mechanism of the urban areas with large orientation angles becomes double-bounce scattering, which is supported by ground reference.

Above all, the component decomposition method using refined volume scattering models and new configurations of compound scattering matrices is a satisfactory decomposition approach, which can be used for the analysis of the scattering mechanism of the land covers.

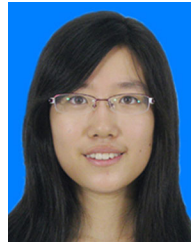
VI. CONCLUSION

In this article, a seven-component decomposition using refined volume scattering models and new configurations of mixed dipoles, namely, M7SD, is proposed. This decomposition method can effectively distinguish the ambiguous regions, especially the buildings with large orientation angles, and overcome the OVS. In the method, refined volume scattering models are proposed and these refined models are introduced to interpret the scattering characteristics of various land covers. According to the refined volume scattering models, the criterion is derived and it is represented in a new way. In this case, the volume scattering power of the buildings with large orientation angles can be distinguished from vegetation areas without the OVS. The experimental results demonstrate that the method is irrelevant to the radar band and the platform, and the proposed method yields satisfactory decomposition results for building areas, especially building areas with large orientation angles. In addition, vegetation areas and orthogonal building areas can be correctly decomposed. Therefore, the proposed method, which overcomes the OVS and mitigates the ambiguity of the scattering mechanism in urban areas, is an effective decomposition approach.

REFERENCES

- [1] D. L. Schuler, J. S. Lee, and G. D. Grandi, "Measurement of topography using polarimetric SAR images," *IEEE Trans. Geosci. Remote Sens.*, vol. 34, no. 5, pp. 1266–1277, Sep. 1996.
- [2] I. Hajnsek, E. Pottier, and S. Cloude, "Inversion of surface parameters from polarimetric SAR," *IEEE Trans. Geosci. Remote Sens.*, vol. 41, no. 4, pp. 727–744, Apr. 2003.
- [3] M. Migliaccio, A. Gambardella, and M. Tranfaglia, "SAR polarimetry to observe oil spills," *IEEE Trans. Geosci. Remote Sens.*, vol. 45, no. 2, pp. 506–511, Feb. 2007.
- [4] A. Bhattacharya and R. Touzi, "Polarimetric SAR urban classification using the Touzi target scattering decomposition," *Can. J. Remote Sens.*, vol. 37, no. 4, pp. 323–332, 2012.
- [5] X. Zhang, W. Dierking, J. Zhang, and J. Meng, "A polarimetric decomposition method for ice in the Bohai sea using c-band PolSAR data," *IEEE J. Sel. Topics Appl. Earth Observ. Remote Sens.*, vol. 8, no. 1, pp. 47–66, Jan. 2015.
- [6] H. Li and W. Perrie, "Sea ice characterization and classification using hybrid polarimetry SAR," *IEEE J. Sel. Topics Appl. Earth Observ. Remote Sens.*, vol. 9, no. 11, pp. 4998–5010, Nov. 2016.
- [7] A. O. Varghese, A. Suryavanshi, and A. K. Joshi, "Analysis of different polarimetric target decomposition methods in forest density classification using c-band SAR data," *Int. J. Remote Sens.*, vol. 37, no. 3, pp. 694–709, 2016.
- [8] L. Huang, B. Tian, Z. Li, and J. Zhou, "Scattering property analysis of supraglacial debris using target decomposition on polarimetric SAR imagery," *IEEE J. Sel. Topics Appl. Earth Observ. Remote Sens.*, vol. 10, no. 5, pp. 1843–1852, May 2017.
- [9] M. A. Merchant, J. R. Adams, A. A. Berg, J. L. Baltzer, W. L. Quinton, and L. E. Chasmer, "Contributions of c-band SAR data and polarimetric decompositions to subarctic boreal peatland mapping," *IEEE J. Sel. Topics Appl. Earth Observ. Remote Sens.*, vol. 10, no. 4, pp. 1467–1482, Apr. 2017.
- [10] A. Buono, F. Nunziata, M. Migliaccio, X. Yang, and X. Li, "Classification of the Yellow River delta area using fully polarimetric SAR measurements," *Int. J. Remote Sens.*, vol. 38, no. 23, pp. 6714–6734, 2017.

- [11] H. Wang, R. Magagi, K. Goïta, M. Trudel, H. McNairn, and J. Powers, "Crop phenology retrieval via polarimetric SAR decomposition and random forest algorithm," *Remote Sens.*, vol. 231, 2019, Art. no. 111234.
- [12] A. Budillon, A. C. Johnsy, and G. Schirrinzi, "Urban tomographic imaging using polarimetric SAR data," *Remote Sens.*, vol. 11, no. 2, p. 132, 2019.
- [13] S. R. Cloude and E. Pottier, "A review of target decomposition theorems in radar polarimetry," *IEEE Trans. Geosci. Remote Sens.*, vol. 34, no. 2, pp. 498–518, Mar. 1996.
- [14] S. R. Cloude, "Target decomposition theorems in radar scattering," *Electron. Lett.*, vol. 21, no. 1, pp. 22–24, 1985.
- [15] S. R. Cloude and E. Pottier, "An entropy based classification scheme for land applications of polarimetric SAR," *IEEE Trans. Geosci. Remote Sens.*, vol. 35, no. 1, pp. 68–78, Jan. 1997.
- [16] S. Guo, X. Qiao, X. Zhang, W. Wang, and F. Du, "Eigenvalue analysis-based approach for Pol-SAR image classification," *IEEE Trans. Geosci. Remote Sens.*, vol. 52, no. 2, pp. 805–818, Feb. 2014.
- [17] A. Freeman and S. L. Durden, "A three-component scattering model for polarimetric SAR data," *IEEE Trans. Geosci. Remote Sens.*, vol. 36, no. 3, pp. 963–973, May 1998.
- [18] Y. Yamaguchi, T. Moriyama, M. Ishido, and H. Yamada, "Four-component scattering model for polarimetric SAR image decomposition," *IEEE Trans. Geosci. Remote Sens.*, vol. 43, no. 8, pp. 1699–1706, Aug. 2005.
- [19] Y. Yamaguchi, A. Sato, W. M. Boerner, R. Sato, and H. Yamada, "Four-component scattering power decomposition with rotation of coherency matrix," *IEEE Trans. Geosci. Remote Sens.*, vol. 49, no. 6, pp. 2251–2258, Jun. 2011.
- [20] S. Zhang *et al.*, "Multiple-component scattering model for polarimetric SAR image decomposition," *IEEE Geosci. Remote Sens. Lett.*, vol. 5, no. 4, pp. 603–607, Oct. 2008.
- [21] D. Xiang, Y. Ban, and S. Yi, "Model-based decomposition with cross scattering for polarimetric SAR urban areas," *IEEE Geosci. Remote Sens. Lett.*, vol. 12, no. 12, pp. 2496–2500, Dec. 2015.
- [22] G. Singh and Y. Yamaguchi, "Model-based six-component scattering matrix power decomposition," *IEEE Trans. Geosci. Remote Sens.*, vol. 56, no. 10, pp. 5687–5704, Oct. 2018.
- [23] G. Singh, Y. Yamaguchi, and S. E. Park, "General four-component scattering power decomposition with unitary transformation of coherency matrix," *IEEE Trans. Geosci. Remote Sens.*, vol. 51, no. 5, pp. 3014–3022, Feb. 2013.
- [24] S. Quan, D. Xiang, B. Xiong, H. Canbin, and K. Gangyao, "A hierarchical extension of general four-component scattering power decomposition," *Remote Sens.*, vol. 9, no. 8, p. 856, 2017.
- [25] H. Li, J. Chen, Q. Li, G. Wu, and J. Chen, "Mitigation of reflection symmetry assumption and negative power problems for the model-based decomposition," *IEEE Trans. Geosci. Remote Sens.*, vol. 54, no. 12, pp. 7261–7271, Dec. 2016.
- [26] S. W. Chen, M. Ohki, M. Shimada, and M. Sato, "Deorientation effect investigation for model-based decomposition over oriented built-up areas," *IEEE Geosci. Remote Sens. Lett.*, vol. 10, no. 2, pp. 273–277, Mar. 2013.
- [27] X. Sun, H. Song, R. Wang, and L. Ning, "High-resolution polarimetric SAR image decomposition of urban areas based on a POA correction method," *Remote Sens. Lett.*, vol. 9, no. 4, pp. 363–372, 2018.
- [28] J. Lee, T. L. Ainsworth, and Y. Wang, "Polarization orientation angle and polarimetric SAR scattering characteristics of steep terrain," *IEEE Trans. Geosci. Remote Sens.*, vol. 56, no. 12, pp. 7272–7281, Dec. 2018.
- [29] G. Singh *et al.*, "Seven-component scattering power decomposition of PolSAR coherency matrix," *IEEE Trans. Geosci. Remote Sens.*, vol. 57, no. 11, pp. 8371–8382, Nov. 2019.
- [30] K. Kitayama, Y. Yamaguchi, J. Yang, and H. Yamada, "Compound scattering matrix of targets aligned in the range direction," *IEICE Trans. Commun.*, vol. 1, pp. 81–88, 2001.
- [31] Y. Wang, W. Yu, C. Wang, and X. Liu, "A modified four-component decomposition method with refined volume scattering models," *IEEE J. Sel. Topics Appl. Earth Observ. Remote Sens.*, vol. 13, pp. 1946–1958, Apr. 2020.
- [32] A. Sato, Y. Yamaguchi, G. Singh, and S. Park, "Four-component scattering power decomposition with extended volume scattering model," *IEEE Geosci. Remote Sens. Lett.*, vol. 9, no. 2, pp. 166–170, Mar. 2012.
- [33] J. S. Lee, M. R. Grunes, E. Pottier, and L. Ferro-Famil, "Unsupervised terrain classification preserving polarimetric scattering characteristics," *IEEE Trans. Geosci. Remote Sens.*, vol. 42, no. 2, pp. 722–731, Apr. 2004.



Yu Wang (Student Member, IEEE) was born in Shandong, China, in 1993. She received the B.S. degree in telecommunication engineering from Jilin University, Jilin, China, in 2016. She is currently working toward the Ph.D. degree in image classification and target decomposition technique for polarimetric synthetic aperture radar and polarimetric interferometric synthetic aperture radar with the University of Chinese Academy of Science, Beijing, China.



Weidong Yu (Member, IEEE) was born in Henan, China, in 1969. He received the M.Sc. and Ph.D. degrees in electrical engineering from the Nanjing University of Aeronautics and Aerospace, Nanjing, China, in 1994 and 1997, respectively.

He has been with the Institute of Electronic, Chinese Academy of Science (IECAS), Beijing, China, since 1997, and became a Professor of communication and information systems, in 2000. He has been the Chief Designer for several SAR systems and is currently the Deputy Director of the Department of

Space Microwave Remote Sensing System, IECAS. He has authored more than 50 papers and holds five patents. His current research interests include airborne and spaceborne SAR system design and their signal processing.



Xiuqing Liu received the graduate degree from the Institute of Electronics, Chinese Academy of Sciences, Beijing, China, in January 2004.

She is currently an Associate Researcher with the Institute of Aerospace Information Innovation of the Chinese Academy of Sciences, Beijing. Her main research interests include polarimetric/compact polarimetric SAR system technology, polarimetric/compact polarimetric SAR data processing, and information extraction.



Chunle Wang received the B.S. degree from Beijing Information Science and Technology University, Beijing, China, in 2008, and the Ph.D. degree from the Graduate University of Chinese Academy of Sciences, Beijing, in 2013.

She is currently working as an Associate Research Assistant about SAR system design and their image processing with the Institute of Electronic, Chinese Academy of Science. Her current research interests include classification and polarimetric target decomposition technique for polarimetric syn-

thetic aperture radar with the University of Chinese Academy of Science, Beijing.